Available online at www.sciencedirect.com
ScienceDirect
Comput. Methods Appl. Mech. Engrg. 410 (2023) 116032
Computer methods in applied mechanics and engineering
www.elsevier.com/locate/cma

Controlling auxeticity in curved-beam metamaterials via a deep generative model

Gerrit Felsch, Naeim Ghavidelnia, David Schwarz, Viacheslav Slesarenko*

Cluster of Excellence livMatS @ FIT – Freiburg Center for Interactive Materials and Bioinspired Technologies, Georges-Köhler-Allee 105, D-79110, Freiburg, Germany

Received 27 January 2023; received in revised form 20 March 2023; accepted 21 March 2023
Available online xxxx

Graphical Abstract

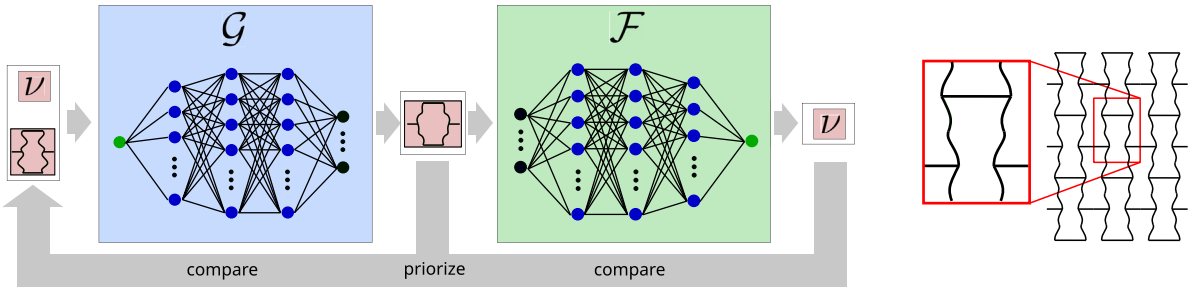

Abstract

Lattice-based mechanical metamaterials are known to exhibit quite a unique mechanical behavior owing to their rational internal architecture. This includes unusual properties such as a negative Poisson's ratio, which can be easily tuned in reentrant-hexagonal metamaterials by adjusting the angles between beams. However, changing the angles also affects the geometrical dimensions of the unit cell. We show that by replacing traditional straight beams with curved ones, it is possible to control Poisson's ratio of reentrant-hexagonal metamaterials keeping their overall dimensions constant. While the mechanical properties of these structures can be predicted through finite element simulations or, in some cases, analytically, many applications require the identification of architectures with specific target properties. To solve this inverse problem, we introduce a deep learning framework for generating metamaterials with desired properties. By supplying the generative model with a guide structure in addition to the target properties, we are able to generate a large number of alternative architectures with the same properties and express a preference for a specific shape. Deep learning predictions, together with experimental measurements, prove that this approach allows us to accurately generate unit cells fitting specific properties for curved-beam metamaterials.

Keywords: Mechanical metamaterials; Inverse design; Machine learning; Auxeticity; Poisson's ratio; Lattices

* Corresponding author.
E-mail address: viacheslav.slesarenko@livmats.uni-freiburg.de (V. Slesarenko).

https://doi.org/10.1016/j.cma.2023.116032

1. Introduction

The extreme mechanical properties and unique behavior of mechanical metamaterials originate in their involved internal organization [1]. One of the most well-known and well-studied manifestations of unusual behavior is a negative Poisson's ratio in so-called auxetics [2]. In contrast to conventional materials that shrink laterally when subjected to uniaxial tension, auxetic materials undergo lateral expansion [3]. The key to the auxetic behavior is hidden in the rational internal architecture often consisting of primitive building blocks — unit cells. While it is possible to combine diverse unit cells within the architecture to achieve specific macroscopic behavior [4–6], traditional auxetic design is usually based on a single unit cell that repeats itself in two or three dimensions [7]. In general, a wide variety of unit cell designs (reentrant [8], chiral [9,10], etc.) in 2D and 3D settings that transform uniaxial elongation to lateral expansion were proposed. Moreover, in 3D settings, unit cells can couple compression and twist deformations [11,12]. It is important to notice, that while elastic constants such as the Poisson's ratio are originally introduced for infinitesimal deformations in isotropic (or orthotropic) materials, a conceptually similar value connecting traversal and lateral deformations has been actively employed to describe mechanical behavior for large deformations [13] or for anisotropic metamaterials [14]. Assuming the applicability of the Poisson's ratio for large deformations, it was shown that it is possible to facilitate a transition from positive to negative Poisson's ratio via elastic buckling [15] or external non-mechanical stimuli [16,17] in mechanical metamaterials.

For traditional mechanical metamaterials [8–10], the geometry of the unit cell univocally defines the overall mechanical behavior. Therefore, it is enough to perform corresponding analysis only for a single unit cell assuming periodic boundary conditions [18–21]. For a wide variety of lattice-based metamaterials with straight beams, the effective mechanical properties were obtained analytically [19] or with the help of numerical simulations [22]. A thoughtful study on the triangular lattices [23] classified them using the symmetry class of the stiffness tensor. Later, for a more general case, the classification of lattices based on their mechanical properties was performed using machine learning [24]. Additionally, an intriguing coupling between normal and shear strains was accounted in a homogenization of chiral metamaterials to describe a coupling between the bulk deformation and bulk rotation of the metamaterial [25,26]. For the classical reentrant-hexagonal unit cell design shown in Fig. 1, analytical solutions for the stiffness matrix were obtained by multiple authors using various homogenization methods and different beam formulations [19,27–34]. In particular, it is established that the metamaterial demonstrates auxetic behavior only if the corresponding angle θ is negative (Fig. 1b); otherwise, the metamaterial possesses a positive Poisson's ratio (Fig. 1a). By harnessing this dependency, metamaterials capable of reversibly switching their auxeticity were realized with the help of stimuli-responsive materials embedded into the architecture [16,35].

While the reentrant-hexagonal architecture provides an easy way for programming its Poisson's ratio via alteration of the angle, such geometrical change affects the overall size of the metamaterial. More specifically, it is impossible to obtain two distinct reentrant-hexagonal metamaterials with different Poisson's ratios that simultaneously share the common overall dimensions and the number of unit cells. In this manuscript, we will reveal how minor modification of the reentrant-hexagonal architecture might enable an extensive range of admissible Poisson's ratios while keeping the dimensions of the unit cell constant. Instead of the classical unit cells shown in Fig. 1, we will consider unit cells constructed with the help of curved beams.

The versatility of the design for non-straight beams and the resulting intriguing interplay between their bending and lateral stiffnesses enable the enriched potential for programming the behavior of mechanical metamaterials through a rational selection of the geometry of the unit cell [36,37]. For example, incorporating Bezier curves in designs has been shown to widen the design space for chiral metamaterials [38] and achieve metamaterials with superior mechanical strength [39]. With the current advances in additive manufacturing [40], the fabrication of lattices with curved beams is not more complicated than the fabrication of classical lattices [41]. While the benefits of curved beams are quite obvious [42,43], their employment in the structure makes the analytical solution for the mechanical behavior of metamaterials much harder [37,44]. Therefore, numerical methods, such as finite element analysis (FEA), are widely used to find corresponding mechanical constants. However, besides a forward problem of obtaining the properties for a specific geometry, from the application point of view, the inverse question of searching for the geometry that will provide the requested mechanical response is even more important. Since multiple curves might generate unit cells with the same properties, the inverse problem becomes ill-posed and requires more advanced solution methods.

The recent development of generative models in machine learning (ML) provides ideas on how to tackle this issue, with variational autoencoders (VAEs) [45] and generative adversarial networks (GANs) [46] having shown

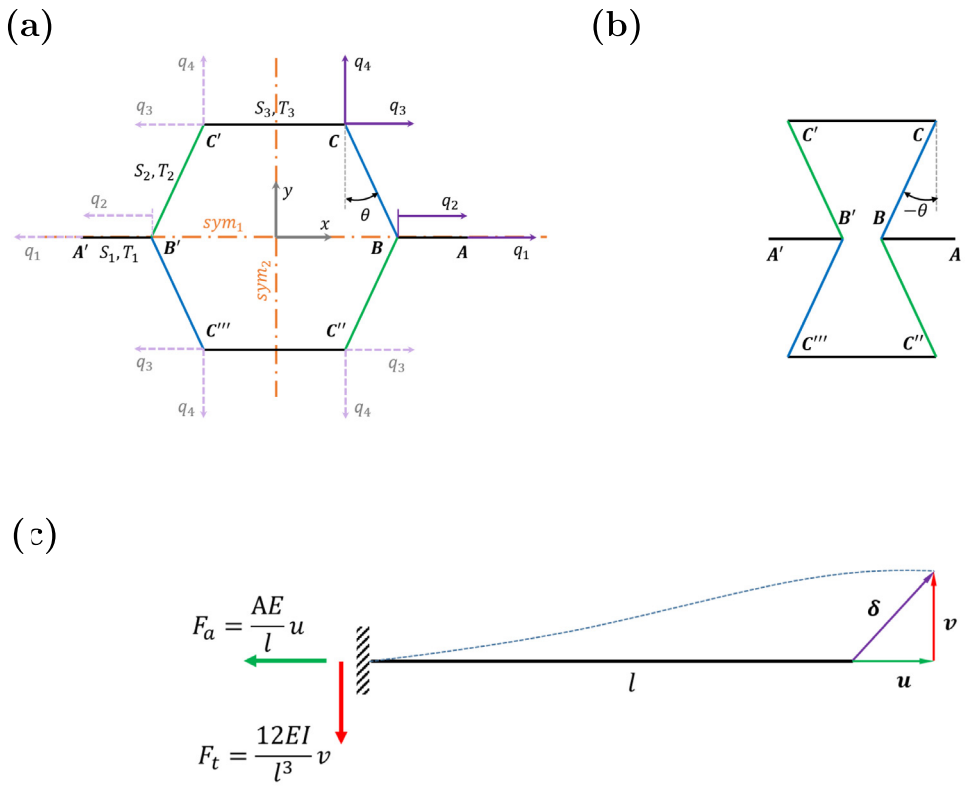

Fig. 1. Classical hexagonal unit cell with its degrees of freedom **(a)**. Classical reentrant unit cell **(b)**. Axial and lateral effective stiffness of the general beam **(c)**.

promising results for the generation of mechanical metamaterials [47,48]. These models learn a transformation to a latent space, where each point corresponds to a valid design. When applied to metamaterials, the dimensions of this space are usually connected to geometric features, which easily allows to interpolate between different designs [47]. However, learning a mapping, where some dimensions reflect mechanical properties instead of geometric features, is computationally expensive, and learning algorithms can be unstable. As an alternative, it has been shown that through the smart design of neural networks and rational selection of the loss functions, it is possible to find a suitable mapping between properties and structure without learning it from scratch [49,50]. In this manuscript, we propose an approach that enables us to efficiently predict the mechanical response of reentrant-hexagonal metamaterials based on curved Bezier beams and, more importantly, efficiently search for a wide variety of geometries that will suffice the specific requirements.

2. Unit cell design

2.1. Classical hexagonal and reentrant lattices

A honeycomb structure is a well-known two-dimensional cellular lattice based on the six-sided hexagonal polygon unit cells with identical strut length and internal angles. Any change in the lengths and angles of the honeycomb structure can lead to a new structure with different mechanical properties. Fig. 1a and 1b illustrate the resultant classical hexagonal and reentrant unit cells by altering the angle of inclined struts (BC) from positive to negative values of θ, which yield a wide range of different structures with positive and negative Poisson's ratios. In this section, a general solution for hexagonal/reentrant structures that consist of various independent lengths and cross sections for beams is derived.

Due to the two symmetrical planes of the unit cell, such as xz (sym_1) and yz (sym_2), the whole deformation of the unit cell under tension or compression in x and y directions could be defined by four individual degrees

of freedoms (q_i, $i = 1, 2, 3, 4$) at A, B and C vertices (Fig. 1a). Because of the symmetrical deformation of unit cell under loading in x and y directions, the similar degrees of freedom are defined at the other vertices (A', B', C', C'' and C'''). According to the equivalency of these degrees of freedom at their corresponding vertices, the deformation of only 1/4 of the unit cell can represent its overall behavior. In addition, the equivalency of the degrees of freedom at the respective vertices captures the periodicity of the unit cell in x and y directions. By considering small deflections and linear material behavior, the overall deformation of the unit cell can be considered as the superposition of separate deformations caused by applying individual loads at each degree of freedom. Therefore, the superposition principle could be implemented for obtaining the system of equations for the unit cell. The system of equilibrium equations for the structure could be written as

$$\begin{Bmatrix} Q_1 \\ Q_2 \\ Q_3 \\ Q_4 \end{Bmatrix} = \begin{pmatrix} k_{11} & k_{12} & k_{13} & k_{14} \\ k_{21} & k_{22} & k_{23} & k_{24} \\ k_{31} & k_{32} & k_{33} & k_{34} \\ k_{41} & k_{42} & k_{43} & k_{44} \end{pmatrix} \begin{Bmatrix} q_1 \\ q_2 \\ q_3 \\ q_4 \end{Bmatrix} \tag{2.1}$$

In this equation, $\{Q\}$ is the force vector which is composed of the external forces acting on the unit cell, $[K]$ is the stiffness matrix of the system and $\{q\}$ is the displacement vector corresponding to each degree of freedom. To calculate the elements of the stiffness matrix of the unit cell based on the superposition method, unit displacements are applied individually to each degree of freedom ($q_i = 1, i = 1, 2, 3, 4$) by constraining all the other degrees of freedom ($q_j = 0, j \neq i$). Due to the symmetrical planes of the hexagonal unit cells, there is no rotational degree of freedom at the joints, which means that the struts of the unit cells are either under elongation (or contraction) or bending (without rotation) at the joints. Therefore, the deformation of an arbitrary strut within the unit cell can be illustrated as shown in Fig. 1c. The general deformation δ at the free end of the beam is decomposed into an axial (u) and a lateral (v) deformation, which yields the corresponding reaction forces (F_a, F_t) at the fixed end of the beam. Based on the Euler–Bernoulli beam theory, the axial and lateral stiffness of the beam can be derived as $S_i = \frac{A_i E}{l_i}$ and $T_i = \frac{12 E I_i}{l_i^3}$ respectively.

By solving the force equilibrium equations for each beam of the unit cell according to the reaction forces resulting from individual degrees of freedom, the stiffness matrix of the unit cell is extracted as follows

$$K = \begin{pmatrix} 2S_1 & -2S_1 & 0 & 0 \\ -2S_1 & 4S_2\sin^2(\theta) + 2S_1 + 4T_2\cos^2(\theta) & -4S_2\sin^2(\theta) - 4T_2\cos^2(\theta) & \sin(\theta)\cos(\theta)\,(4S_2 - 4T_2) \\ 0 & -4S_2\sin^2(\theta) - 4T_2\cos^2(\theta) & 4S_2\sin^2(\theta) + 4S_3 + 4T_2\cos^2(\theta) & \sin(\theta)\cos(\theta)\,(4T_2 - 4S_2) \\ 0 & \sin(\theta)\cos(\theta)\,(4S_2 - 4T_2) & \sin(\theta)\cos(\theta)\,(4T_2 - 4S_2) & 4S_2\cos^2(\theta) + 4T_2\sin^2(\theta) \end{pmatrix} \tag{2.2}$$

After deriving the stiffness matrix of the unit cell, the system of equations (Eq. (2.1)) can be solved for different loading conditions. To obtain the mechanical properties of the hexagonal structure in y direction, the corresponding loading condition is applied to the unit cell, and the system of equations is solved to find the resultant deformations at the defined degrees of freedom. By applying $Q_4 = 1$ ($Q_{1,2,3} = 0$), the Poisson's ratio in y direction $\nu := \nu_{yx} = -\varepsilon_x/\varepsilon_y$ can be found via components of K(2.2). The strains in x and y directions (ϵ_x and ϵ_y) are calculated using the results of q_1 and q_4 for their corresponding loading condition as follow:

$$\begin{cases} \epsilon_x = \dfrac{q_1}{W_{uc}} \\ \epsilon_y = \dfrac{q_4}{H_{uc}} \end{cases} \tag{2.3}$$

where the H_{uc} and W_{uc} stand for the total height and width of the unit cell and can be calculated as $H_{uc} = 2l_2\cos(\theta)$ and $W_{uc} = l_2\sin(\theta) + 2l_1$ respectively.

By solving the system of equations ($\{Q\} = [K]\{q\}$) for loading condition of $Q_4 = 1$, $Q_{1,2,3} = 0$ and calculating the $\{q\}$ vector, the final relationship for Poisson's ratio of the unit cell is written as follows:

$$\nu_{yx} = -\frac{q_1}{q_4}.\frac{H_{uc}}{W_{uc}} = -\frac{2l_2\sin(\theta)\cos^2(\theta)\,(T_2 - S_2)}{S_2T_2\,(l_2\sin(\theta) + 2l_1)\left(\dfrac{\cos^2(\theta)}{S_2} + \dfrac{\sin^2(\theta)}{T_2}\right)} \tag{2.4}$$

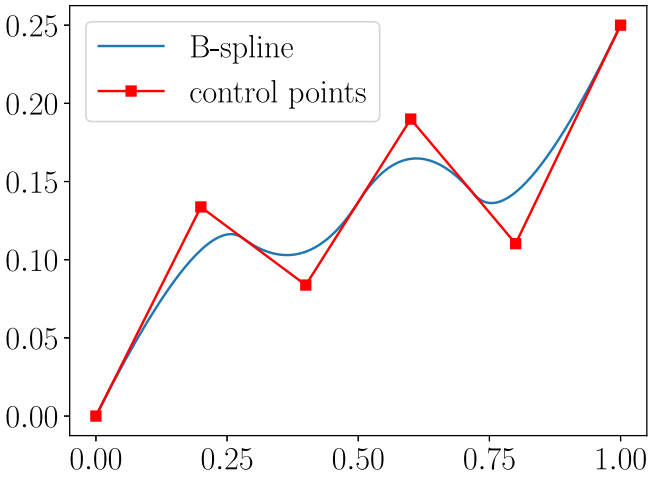

Fig. 2. A quadratic ($p = 2$) B-spline build from the six control points ($c_i, i = 1, \ldots, 6$) and the knot vector $k = (0, 0, 0, 0.2, 0.5, 0.8, 1, 1, 1)$.

The aforementioned results are used to calculate the Poisson's ratio of hexagonal structures by using positive values of θ, or reentrant structures by substitution of negative values of θ. The Poisson's ratio clearly depends on both the axial and lateral stiffness of the horizontal and inclined beams. Varying these stiffnesses by substituting the classical straight beams with curved beams, a huge design variability can be achieved.

2.2. Bezier curve theory

To replace straight beams with complex curved elements, a suitable representation of these elements is needed. B-splines are able to provide smooth parametric descriptions of such elements. By definition, these B-spline curves $B(t)$ are constructed from a combination of so-called control points and several basis functions of order p [51]. One such B-spline and the corresponding control points $c_i \in \mathbb{R}^d$ are shown in Fig. 2. Each point $t \in [0, 1]$ along the curve is given by a weighted sum of the control points, where the weights are defined by the basis functions $N_{i,p} : [0, 1] \to [0, 1]$ as

$$B(t) = \sum_{i=1}^{n} N_{i,p}(t) c_i \tag{2.5}$$

This method assures that some parts of the curve are more dependent on certain control points than others, which gets more evident when looking at the way the basis functions themselves are constructed via recursion. First, the curve is partitioned into smaller intervals, divided by knots k_i, $i = 1, \ldots, n + p + 1$, $k_i \leq k_{i+1}$. Each zero-order basis ($p = 0$) function is defined as

$$N_{i,0}(t) = \begin{cases} 1 & \text{if } k_i < t < k_{i+1} \\ 0 & \text{otherwise} \end{cases} \tag{2.6}$$

As one can see, the basis functions of order 0 are not smooth. The recursive step then performs a smoothing operation on each base function using one neighboring function, giving continuous curves

$$N_{i,p}(t) = \frac{t - k_i}{k_{i+p} - k_i} N_{i,p-1}(t) + \frac{k_{i+p+1} - t}{k_{i+p+1} - k_{i+p}} N_{i+1,p-1}(t) \tag{2.7}$$

As can be seen, the number of control points contributing to each point of the curve increases with the order. Fig. 2 shows a quadratic spline ($p = 2$) where this number is usually three. However, the start and end points of the curve each depend only on a single control point. For this to occur, it is necessary to have $p + 1$ knots with $k_i = k_0$ and $k_i = k_{n+p+1}$, respectively. In this case, Eq. (2.5) yields $B(0) = c_1$ and $B(1) = c_n$. To generate the B-splines for the unit cells, we used the Python-package Splipy [52].

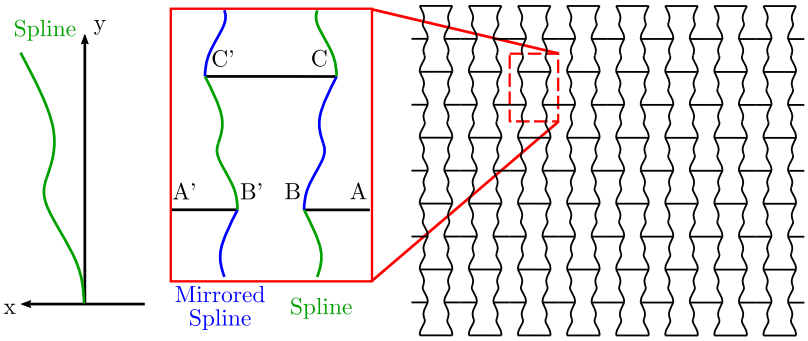

Fig. 3. A B-spline, the corresponding representative unit cell and a resulting system comprised of 8 × 5 representative unit cells.

2.3. Generated metamaterials

The unit cells of the metamaterials considered here are inspired by hexagonal and reentrant honeycomb structures. As can be seen in Fig. 3, the horizontal struts are connected by a curved quadratic B-spline or its mirrored equivalent instead of straight beams. Due to the periodicity, there are several ways to pick a unit cell for the same lattice; the unit cell shown in Fig. 3 is just one of them. Like the one shown in Fig. 2, the B-spline connecting the horizontal struts is given by six control points. As the unit cell is univocally defined by the B-spline, these points can be further used to represent the whole unit cell. For simplification, control points were placed equidistantly along the y-axis, leaving only the coordinates along the x-axis as design variables. Additionally, the length of the horizontal struts (AB in Fig. 3) was kept the same for all unit cells, leaving them only dependent on the relative position of the control points. The first control point was always selected as (0,0). Therefore, each structure is given by a set of five independent parameters — the vertical values $c_{i,y}$ of the control points c_i, $i = 2, \ldots, 6$ (see Fig. 2). Using these parameters as design variables, two different datasets were created:

- *Set 1* consists of pairs (x_i, y_i) of unit cells based on B-splines with a fixed endpoint (x_i) and the corresponding Poisson's ratio (y_i). Fixing the end results in unit cells corresponding to variations of a single reentrant unit cell design with $B'B = 0.5\ C'C$. For this dataset, the horizontal struts always have the same relative position, leaving the variation of the B-splines as the only source of properties differences.
- *Set 2* consists of pairs (x_i, y_i) of unit cells based on B-splines with free endpoints (x_i) and the corresponding Poisson's ratio (y_i). Free ends result in a greater diversity of unit cells. As can be seen in Fig. 4, varying the x-coordinate of the end of the unit cell can change its underlying geometry from more reentrant-like to hexagonal (see the dashed red lines in Fig. 4b).

To obtain the Poisson's ratio for the structures in both datasets, numerical simulations were performed in the finite element (FE) package COMSOL 5.4a via the LiveLink interface. For these simulations, the B-splines were discretized into 150 beam elements. Periodicity was prescribed by matching the displacements and angles on the boundaries of the unit cell. The Poisson's ratio was found as the ratio between lateral expansion vs applied tensile strain ($\nu = -\varepsilon_x/\varepsilon_y$). Note that the considered metamaterials are not isotropic, therefore the value of this Poisson's ratio is not bounded by 0.5, as in case of isotropic materials. To verify the simulation approach, results for unit cells with straight beams were compared to theoretical values of ν_{yx} obtained via Eq. (2.4). It was found that simulations match the theory well for small deformations, as shown in Fig. 5.

3. ML implementation for forward (structure–property) problem

The Neural Network (NN) model $\mathcal{F}$ depicted in Fig. 6a is introduced as a surrogate model for the FE simulation. By training on structure–property pairs, the neural network learns to emulate the simulation in predicting the Poisson's ratio of a structure and thus to solve the forward problem. The surrogate model allows efficient computation of the shape derivatives necessary for training the inverse model through the backpropagation algorithm [53].

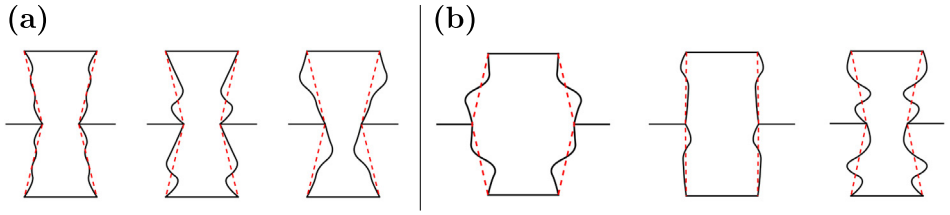

Fig. 4. Unit cell examples from *Set 1* **(a)** and *Set 2* **(b)**. While the dimensions of the unit cells from *Set 1* are constant, cells from *Set 2* can resemble both reentrant or hexagonal structures. (For interpretation of the references to color in this figure legend, the reader is referred to the web version of this article.)

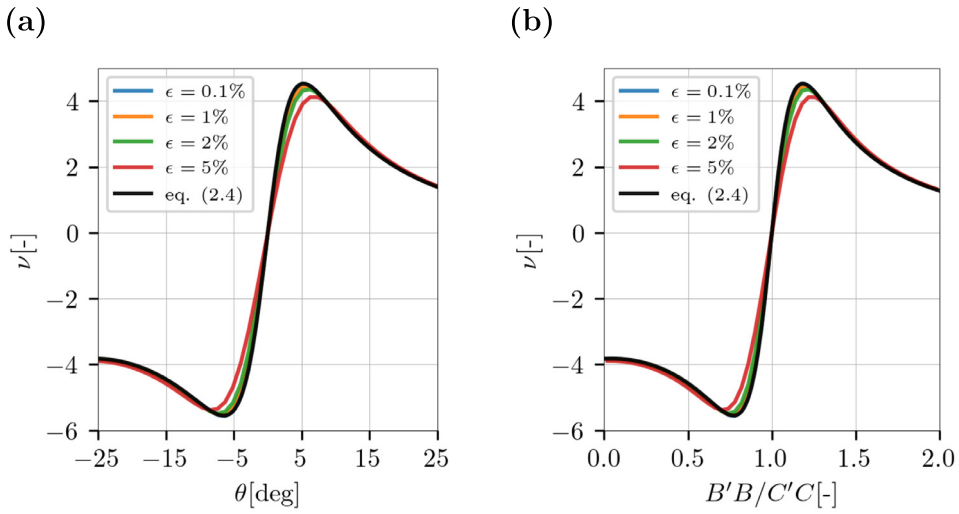

Fig. 5. The Poisson's ratios (ν) of different unit cells with straight beams (as shown in Fig. 1a–b) depending on angle θ **(a)** and the ratio between $B'B$ and $C'C$ **(b)** respectively. The black curve corresponds to Eq. (2.4), while the others were obtained through simulations in COMSOL with varying applied strain (ε). Note, that simulations match the theory well, especially for small strain.

Information about the structure is passed to the neural network as the five constitutive parameters of the corresponding B-spline. The network consists of four fully connected layers, including the output layer, where each hidden layer is followed by a ReLU activation function. To learn how to predict the Poisson's ratio, the network was trained using the Adam optimizer [54] and a Mean Squared Error objective function. Layer normalization [55] was used to reduce training time. For both datasets, the Poisson's ratios and the B-spline parameters were rescaled to the range [0,1]. For each of the two datasets, a separate instance of the network $\mathcal{F}$ was trained.

3.1. Set 1

Of the 25,000 examples in *Set 1*, 90% were used for training, while the remaining 10% were used as test set. Fig. 7a shows the comparison between the Poisson's ratios obtained by the FEA and the forward model $\mathcal{F}$ for both the train and test parts of *Set 1*. Predictions of the network are very close to simulation results, and a good generalization can be observed with data from train and test sets showing similar distributions ($R^2 = 0.99984$).

3.2. Set 2

Set 2 consists of 25,000 data points, of which again 90% were used for training and 10% for testing. Fig. 7b shows the comparison between the Poisson's ratio calculated through FEA and the value predicted by the network. As for the optimal model, the predicted value should match the one from simulation, so ideally the plot would yield

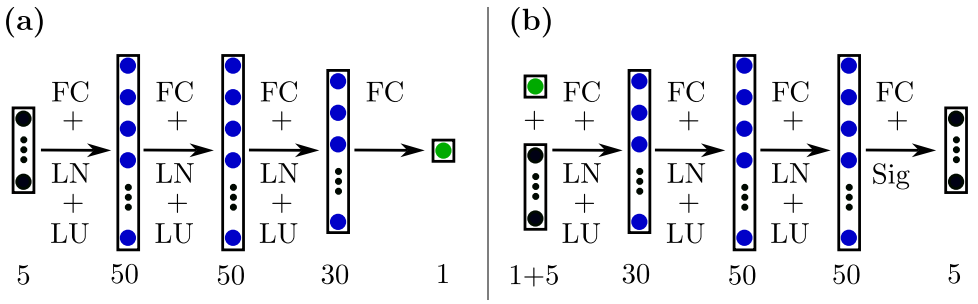

Fig. 6. The forward NN model $\mathcal{F}$ **(a)** and the inverse NN model $\mathcal{G}$ **(b)**. The different layers are color coded. Poisson's ratios are shown in green, B-splines in black and hidden layers in blue. The hidden layers consist of fully connected (FC), layer normalization (LN) layers in combination with LeakyReLU (LU) and Sigmoid (Sig) activation functions. (For interpretation of the references to color in this figure legend, the reader is referred to the web version of this article.)

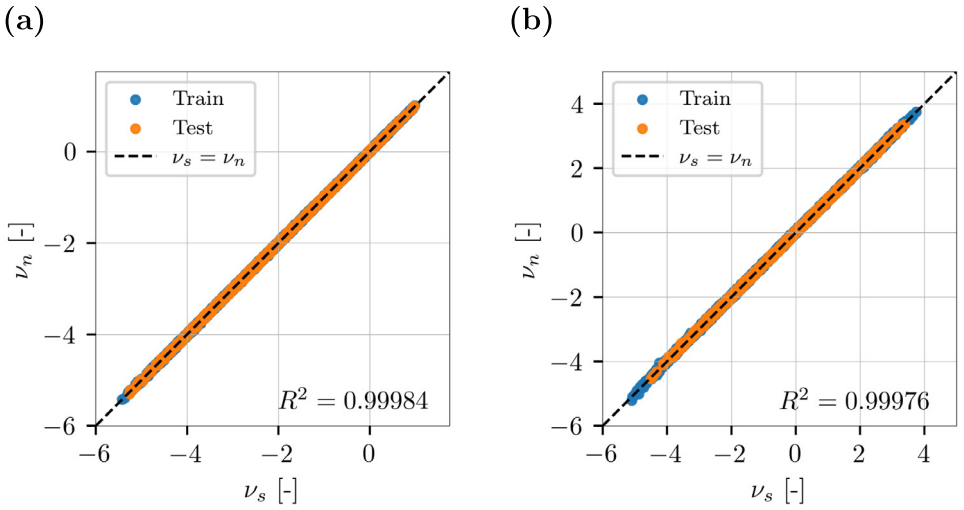

Fig. 7. Comparison between the Poisson's ratios obtained by FEA (ν_s) and the forward NN model $\mathcal{F}$ (ν_n) for training and testing data from *Set 1* **(a)** and *Set 2* **(b)**.

a line with a unit slope. Similar to *Set 1* the model generalizes properly, with test set performance equivalent to the training set ($R^2 = 0.99976$).

The obtained models show an extremely good prediction of the mechanical properties even with a relatively small number of samples. However, for both datasets, multiple unit cells can yield the same Poisson's ratio. This causes the inverse problem to be ill-posed, as multiple solutions exist for a single input.

4. ML implementation for inverse (property–structure) problem

Predicting a curve that fits given properties is far more challenging than solving the forward problem described in the previous section. It is not possible to simply reverse $\mathcal{F}$ and train this network on property/structure pairs as there are multiple curves that fit the same property. Instead, the reversed network needs to be modified to address the following three major challenges, yielding a complex architecture consisting of interconnected inverse $\mathcal{G}$ (see Fig. 6b) and forward $\mathcal{F}$ (see Fig. 6a) models.

(1) Neural networks always produce the same output for the same input; they are deterministic. This also means that multiple possible structures fitting the same input properties disturb the training process preventing the network from learning. A common approach to avoid this is to utilize the pretrained surrogate model $\mathcal{F}$ [49]. Using $\mathcal{F}$, it is possible to directly compare the target properties to the ones of the generated structure and create a mapping

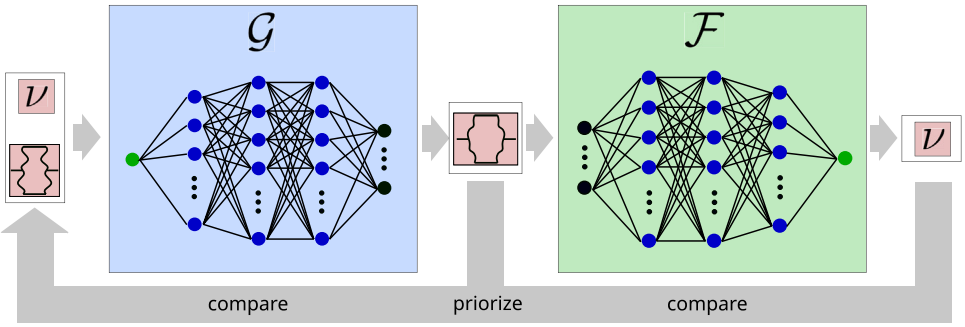

Fig. 8. Schematic of the inverse design system. The generative model $\mathcal{G}$ receives a target Poisson's ratio and guide curve. Based on these it generates a unit cells defined by a B-spline. This B-spline is then fed to the forward model $\mathcal{F}$ which estimates the Poisson's ratio of the generated structure so it can be compared to the target one for training.

without multiple solutions. This allows further to backpropagate corresponding property-based loss through $\mathcal{F}$ to the generator network $\mathcal{G}$.

(2) While the utilization of $\mathcal{F}$ allows training of $\mathcal{G}$, each input still yields only one output, meaning that only one structure can be generated for each distinct property input. To allow multiple solutions, additional inputs need to be employed, providing a criterion for choosing from the possible solutions. For this, the additional inputs have to be connected to the generated structure, or $\mathcal{G}$ will simply learn to ignore them. Such a connection can be learned as well (for example, by training a Generative Adversarial Network [46]), which requires a lot of additional effort but allows the additional inputs to be completely random (i.e., noise). However, here the additional input is provided in the form of a so-called guide curve. A guide curve is an arbitrarily chosen structure that does not have to fit the target properties. The generator $\mathcal{G}$ is trained to generate the structure fitting the target properties that most closely resembles the guide curve. This way, different structures are generated for different guide curves, and it is possible to express a preference for a certain shape. Introducing the guide curve and combining $\mathcal{F}$ and $\mathcal{G}$ yields the system shown in Fig. 8.

(3) As neural networks are usually not able to make accurate predictions outside of the range of their training data, it is necessary to limit generated structures to a sensible range when fitting the inverse model $\mathcal{G}$. Here an additional term was added to the loss function, that penalizes solutions which differ much from a straight line between start and endpoint.

Each of these challenges is addressed by a distinct term of the following loss function:

$$\min_{\mathcal{G}} \mathcal{O}(\mathcal{F},\mathcal{G}) = \underbrace{\frac{1}{n}\sum_{i=1}^{n}(\mathcal{F}(\mathcal{G}(\mathbf{x}_i,\mathbf{y}_i))-\mathbf{y}_i)^2}_{(1)} + \alpha \underbrace{\frac{1}{n}\sum_{i=1}^{n}(\mathcal{G}(\mathbf{x}_i,\mathbf{y}_i)-\mathbf{x}_i)^2}_{(2)} + \underbrace{\frac{1}{n}\sum_{i=1}^{n}\sum_{j=1}^{n_c}\mathbb{1}_{d_j>K}\; d_j}_{(3)}, \tag{4.1}$$

where n is the number of samples, n_c the number of control points, $d_j = (\mathcal{G}(\mathbf{x}_i)_j - \frac{j-1}{n_c-1}c_{n_c})^2$ the deviation of the B-spline from a straight line and K a threshold for penalizing this deviation.

In Eq. (4.1) the parameter α controls the trade-off between matching the target properties or matching the guide curve (see the left side of Fig. 8). For training the inverse model $\mathcal{G}$, both target properties and guide curve were sampled from random uniform distributions. Note that the guide curve is an arbitrary curve that might be not represented in the dataset. The network shown in Fig. 6b was trained separately on *Set 1* and *Set 2*, each time combined with the respective forward model. For *Set 1*, the endpoints of the guide curves as well as the ones of the generated B-splines were fixed. Similar to training the forward model, Adam was used as an optimizer.

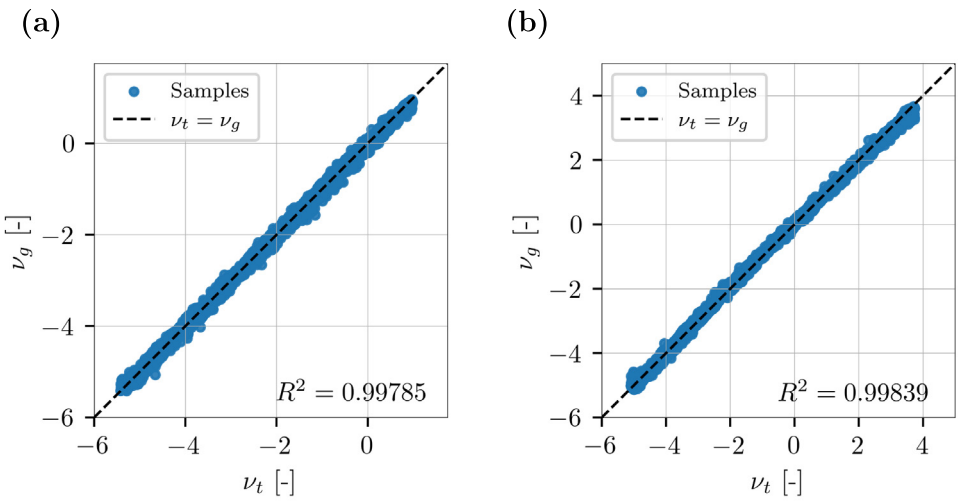

Fig. 9. Comparison between the target Poisson's ratios (ν_t) and the Poisson's ratios of the corresponding structures generated by $\mathcal{G}$ (ν_g) for *Set 1* **(a)** and *Set 2* **(b)**.

Fig. 9 shows the comparison between target and resulting mechanical properties (Poisson's ratio) for randomly picked guide curves. The target properties were chosen randomly, while the resulting Poisson's ratios of the corresponding generated curves were obtained through FEA. A good fitting ($R^2 = 0.99785$ for *Set 1* and $R^2 = 0.99839$ for *Set 2*) was obtained, although $\mathcal{G}$ was not directly trained on FEA data, but $\mathcal{F}$ instead. As expected, the inverse model trained on *Set 2* can design unit cells with a greater variety of properties than the model trained on *Set 1*.

Since $\mathcal{G}$ has two inputs (target Poisson's ratio and guide curve), we can demonstrate the performance of the inverse network in two different ways. Fig. 10a–b show the variety of curves generated for the same guide curve with different target Poisson's ratio. It can be observed that a continuous change in Poisson's ratio usually leads to quite smooth transformations in the resulting curves. However, for some values of Poisson's ratio, one cannot maintain the similarity with the guide curve. This is in part due to the additional constraint on the "width" of the curve (see the last term in Eq. (4.1)).

Similarly, Fig. 10c–d show the variety of the generated curves with the same properties, but based on the different guide curves. It can be observed that the variety of the admissible generated curves with the same Poisson's ratio is immense. Note that the model trained on *Set 2* shows a wider variety of curves and Poisson's ratios as compared to the model trained on *Set 1*. This is expected behavior since geometrically *Set 1* is the subset of *Set 2*, which includes unit cells based on hexagonal elements ($\theta > 0$) besides of reentrant ones.

5. Experiments

To validate the finite element simulation, mechanical tests were performed on ten different geometries. While nine out of these ten specimens were based on unit cells generated by the inverse model $\mathcal{G}$ for *Set 1*, the tenth sample was based on the corresponding reentrant unit cell with straight beams for reference. These specimens (see Fig. 11a) consisted of 5 × 5 unit cells (25 mm × 18.75 mm × 5 mm each) were additively manufactured from Ninjaflex® TPU filament by a Creality CR-10 3D-Printer. The tensile behavior of the samples was tested on a Zwick&Roell 10kN universal testing machine. Since the purpose of these tests was to verify how well the real specimens fit the target Poisson's ratio, specimens included structures with both auxetic and non-auxetic behavior. To minimize viscoelastic effects and assure conditions as close to the simulations as possible, samples were subjected to a tensile load with a slow rate of 20 mm/min. The resulting Poisson's ratio was determined as quotient of lateral and applied strain at 1% total strain. The measurements necessary for this calculation were taken by analyzing captured videos of the experiments in the software Fiji [56].

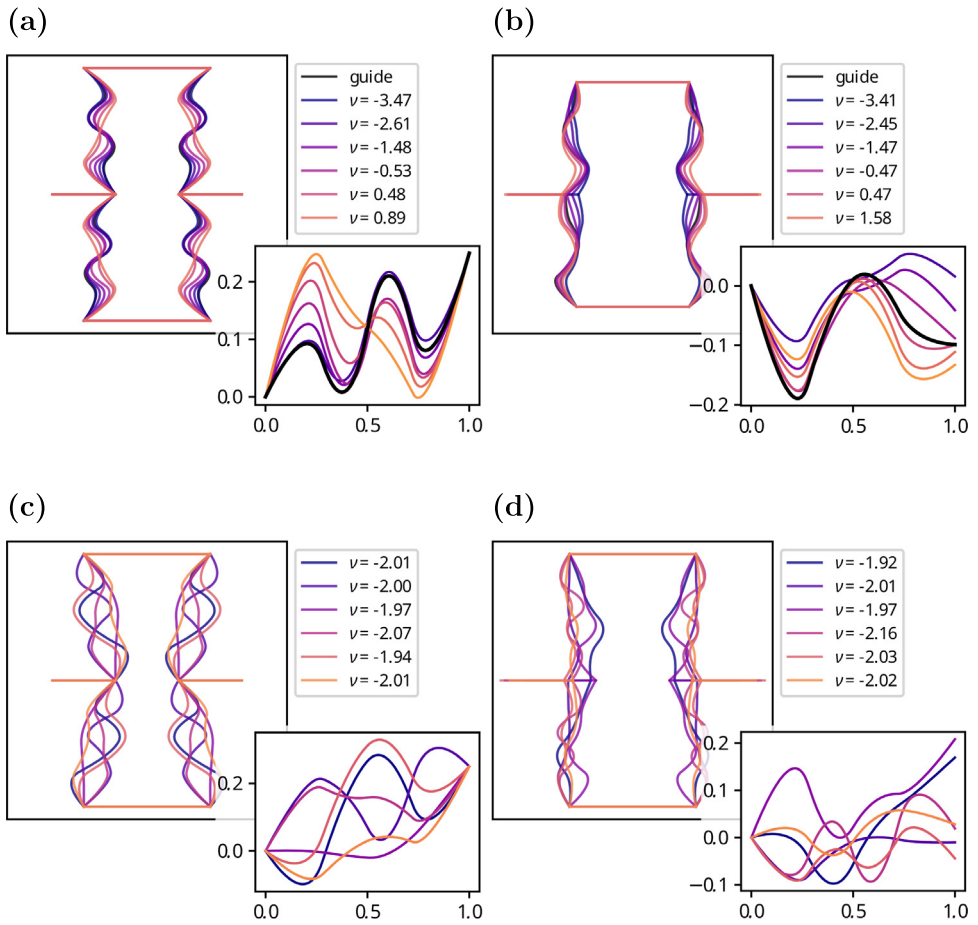

Fig. 10. Generated unit cells and corresponding B-splines for variation of target Poisson's ratio with the same guide curve for *Set 1* **(a)** and *Set 2* **(b)**. Similarly, the generated unit cells and corresponding B-splines for variation of the guide curve while keeping the target Poisson's ratio the same for *Set 1* **(c)** and *Set 2* **(d)**.

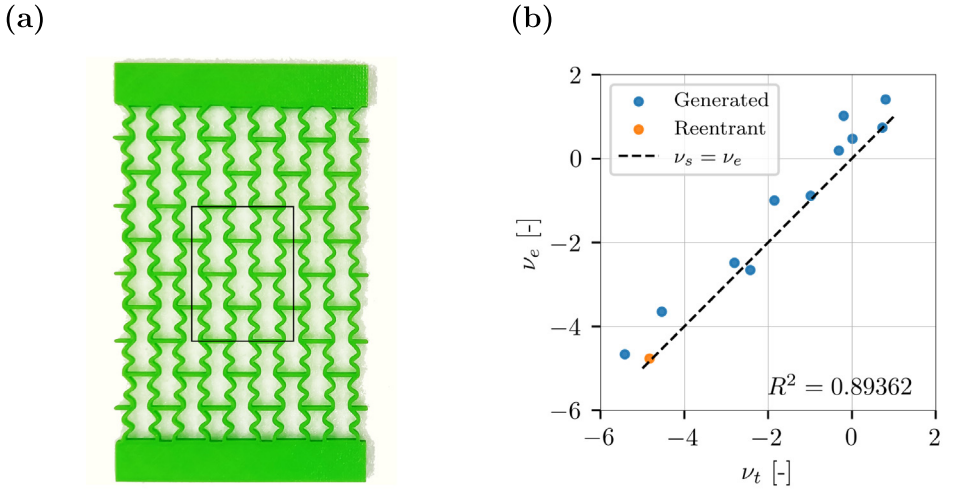

Fig. 11. An exemplary test specimen **(a)**. Comparison between the target Poisson's ratios (ν_t) and the Poisson's ratios derived from the experiments (ν_e) **(b)**.

The test results shown in Fig. 11b display a clear correlation between target and exhibited behavior. This means that despite being only trained on synthetic data, our model is able to make reliable predictions in a real world setting.

6. Conclusion

In this work, we introduced a class of reentrant-hexagonal metamaterials based on curved Bezier beams and a corresponding deep learning framework to generate unit cells with desired mechanical properties. Using Bezier curves instead of straight beams allowed us to obtain a variety of different properties while keeping the dimensions of the corresponding unit cells constant. At the same time, it yields a large number of possible unit cells to fit given properties. We used a guide curve instead of noise to create a one-on-one mapping for this inverse problem. This approach enables us not only to generate several unit cells with the same properties, but also to express a preference for a specific shape.

As the proposed forward neural network model can reliably predict mechanical properties of metamaterials ($R^2 > 0.999$), the corresponding inverse model was able to accurately generate unit cells fitting specific properties ($R^2 > 0.997$). Experiments demonstrated that this ability extends to a real world setting, even though both models were trained on simulations. Furthermore, both models are computationally efficient, allowing us to generate a large number of unit cells in a short amount of time (around 20,000 unit cells per second).

Declaration of competing interest

The authors declare that they have no known competing financial interests or personal relationships that could have appeared to influence the work reported in this paper.

Data availability

Data will be made available on request.

Acknowledgments

Funded by the Deutsche Forschungsgemeinschaft (DFG, German Research Foundation) under Germany's Excellence Strategy – EXC-2193/1 – 390951807. The authors acknowledge support by the state of Baden-Württemberg through bwHPC and the German Research Foundation (DFG) through grant no INST 39/963-1 FUGG (bwForCluster NEMO).

References

[1] A.A. Zadpoor, Mechanical meta-materials, Mater. Horiz. 3 (5) (2016) 371–381.
[2] H.M.A. Kolken, A.A. Zadpoor, Auxetic mechanical metamaterials, RSC Adv. 7 (9) (2017) 5111–5129.
[3] X. Ren, R. Das, P. Tran, T.D. Ngo, Y.M. Xie, Auxetic metamaterials and structures: a review, Smart Mater. Struct. 27 (2) (2018) 023001.
[4] J.K. Wilt, C. Yang, G.X. Gu, Accelerating auxetic metamaterial design with deep learning, Adv. Eng. Mater. 22 (5) (2020) 1901266.
[5] M.J. Mirzaali, J. Shahram, S. Matteo, L.M. Vergani, A.A. Zadpoor, Shape-matching soft mechanical metamaterials, Sci. Rep. 8 (1) (2018) 965.
[6] Z. Zhang, A.O. Krushynska, Programmable shape-morphing of rose-shaped mechanical metamaterials, APL Mater. 10 (8) (2022) 080701.
[7] X. Zheng, H. Lee, T.H. Weisgraber, M. Shusteff, J. DeOtte, E.B. Duoss, J.D. Kuntz, M.M. Biener, Q. Ge, J.A. Jackson, S.O. Kucheyev, N.X. Fang, C.M. Spadaccini, Ultralight, ultrastiff mechanical metamaterials, Science 344 (6190) (2014) 1373–1377.
[8] C. Korner, Y. Liebold-Ribeiro, A systematic approach to identify cellular auxetic materials, Smart Mater. Struct. 24 (2) (2015) 25013.
[9] J. Reinbold, T. Frenzel, A. Münchinger, M. Wegener, The rise of (chiral) 3D mechanical metamaterials, Materials 12 (21) (2019) 3527.
[10] W. Wu, W. Hu, G. Qian, H. Liao, X. Xu, F. Berto, Mechanical design and multifunctional applications of chiral mechanical metamaterials: A review, Mater. Des. 180 (2019) 107950.
[11] T. Frenzel, M. Kadic, M. Wegener, Three-dimensional mechanical metamaterials with a twist, Science 358 (6366) (2017) 1072–1074.
[12] I. Fernandez-Corbaton, C. Rockstuhl, P. Ziemke, P. Gumbsch, A. Albiez, R. Schwaiger, T. Frenzel, M. Kadic, M. Wegener, New twists of 3D chiral metamaterials, Adv. Mater. 31 (26) (2019) 1807742.
[13] B. Ling, K. Wei, Z. Wang, X. Yang, Z. Qu, D. Fang, Experimentally program large magnitude of Poisson's ratio in additively manufactured mechanical metamaterials, Int. J. Mech. Sci. 173 (2020) 105466.

[14] M.J. Mirzaali, A. Caracciolo, H. Pahlavani, S. Janbaz, L. Vergani, A. Zadpoor, Multi-material 3D printed mechanical metamaterials: Rational design of elastic properties through spatial distribution of hard and soft phases, Appl. Phys. Lett. 113 (24) (2018) 241903.
[15] J. Li, V. Slesarenko, S. Rudykh, Auxetic multiphase soft composite material design through instabilities with application for acoustic metamaterials, Soft Matter 14 (30) (2018) 6171–6180.
[16] O. Skarsetz, V. Slesarenko, A. Walther, Programmable auxeticity in hydrogel metamaterials via shape-morphing unit cells, Adv. Sci. 9 (23) (2022) 2201867.
[17] Q. He, Z. Wang, Y. Wang, Z. Wang, C. Li, R. Annapooranan, J. Zeng, R. Chen, S. Cai, Electrospun liquid crystal elastomer microfiber actuator, Science Robotics 6 (57) (2021) eabi9704.
[18] L. Mizzi, D. Attard, R. Gatt, K.K. Dudek, B. Ellul, J.N. Grima, Implementation of periodic boundary conditions for loading of mechanical metamaterials and other complex geometric microstructures using finite element analysis, Eng. Comput. 37 (3) (2021) 1765–1779.
[19] N. Karathanasopoulos, F. Dos Reis, H. Reda, J.F. Ganghoffer, Computing the effective bulk and normal to shear properties of common two-dimensional architectured materials, Comput. Mater. Sci. 154 (2018) 284–294.
[20] M. Ryvkin, V. Slesarenko, A. Cherkaev, S. Rudykh, Fault-tolerant elasticplastic lattice material, Phil. Trans. R. Soc. A (2020) 20190107.
[21] J. Ganghoffer, I. Goda, A. Novotny, R. Rahouadj, J. Sokolowski, Homogenized couple stress model of optimal auxetic microstructures computed by topology optimization, ZAMM Z. Angew. Math. Mech. 98 (5) (2018) 696–717.
[22] N. Karathanasopoulos, F. Dos Reis, P. Hadjidoukas, J.F. Ganghoffer, LatticeMech: A discrete mechanics code to compute the effective static properties of 2D metamaterial structures, SoftwareX 11 (2020) 100446.
[23] M.L.M. François, L. Chen, M. Coret, Elasticity and symmetry of triangular lattice materials, Int. J. Solids Struct. 129 (2017) 18–27.
[24] R. Kulagin, Y. Beygelzimer, Y. Estrin, A. Schumilin, P. Gumbsch, Architectured lattice materials with tunable anisotropy: Design and analysis of the material property space with the aid of machine learning, Adv. Eng. Mater. 22 (12) (2020) 2001069.
[25] A. Bacigalupo, L. Gambarotta, Homogenization of periodic hexa- and tetrachiral cellular solids, Compos. Struct. 116 (2014) 461–476.
[26] N. Karathanasopoulos, F. Dos Reis, M. Diamantopoulou, J.F. Ganghoffer, Mechanics of beams made from chiral metamaterials: Tuning deflections through normal-shear strain couplings, Mater. Des. 189 (2020) 108520.
[27] N. Ghavidelnia, M. Bodaghi, R. Hedayati, Idealized 3D auxetic mechanical metamaterial: An analytical, numerical, and experimental study, Materials 14 (4) (2021) 993.
[28] K. El Nady, F. Dos Reis, J. Ganghoffer, Computation of the homogenized nonlinear elastic response of 2D and 3D auxetic structures based on micropolar continuum models, Compos. Struct. 170 (2017) 271–290.
[29] F. Dos Reis, J. Ganghoffer, Construction of micropolar continua from the asymptotic homogenization of beam lattices, Comput. Struct. 112 (2012) 354–363.
[30] N. Karathanasopoulos, H. Reda, J.-f. Ganghoffer, Designing two-dimensional metamaterials of controlled static and dynamic properties, Comput. Mater. Sci. 138 (2017) 323–332.
[31] R. Hedayati, N. Ghavidelnia, M. Sadighi, M. Bodaghi, Improving the accuracy of analytical relationships for mechanical properties of permeable metamaterials, Appl. Sci. 11 (3) (2021) 1332.
[32] S. Mukherjee, S. Adhikari, A general analytical framework for the mechanics of heterogeneous hexagonal lattices, Thin-Walled Struct. 167 (2021) 108188.
[33] I.E. Berinskii, In-plane elastic properties of auxetic multilattices, Smart Mater. Struct. 27 (7) (2018) 075012.
[34] I. Berinskii, Elastic in–plane properties of cellular materials: Discrete approach, Mech. Mater. 148 (2020) 103501.
[35] Z. Wang, Z. Wang, Y. Zheng, Q. He, Y. Wang, S. Cai, Three-dimensional printing of functionally graded liquid crystal elastomer, Sci. Adv. 6 (39) (2020) eabc0034.
[36] Y. Fu, W. Liu, Design of mechanical metamaterial with controllable stiffness using curved beam unit cells, Compos. Struct. 258 (2021) 113195.
[37] S. Mukherjee, S. Adhikari, The in-plane mechanics of a family of curved 2D lattices, Compos. Struct. 280 (2022) 114859.
[38] A. Álvarez-Trejo, E. Cuan-Urquizo, A. Roman-Flores, L. Trapaga-Martinez, J. Alvarado-Orozco, Bézier-based metamaterials: Synthesis, mechanics and additive manufacturing, Mater. Des. 199 (2021) 109412.
[39] S. Lee, Z. Zhang, G. X. Gu, Generative machine learning algorithm for lattice structures with superior mechanical properties, Mater. Horiz. 9 (3) (2022) 952–960.
[40] X. Yuan, M. Chen, Y. Yao, X. Guo, Y. Huang, Z. Peng, B. Xu, B. Lv, R. Tao, S. Duan, H. Liao, K. Yao, Y. Li, H. Lei, X. Chen, G. Hong, D. Fang, Recent progress in the design and fabrication of multifunctional structures based on metamaterials, Curr. Opin. Solid State Mater. Sci. 25 (1) (2021) 100883.
[41] J.B. Pascual-Francisco, L.I. Farfan-Cabrera, E. Cuan-Urquizo, A. Álvarez-Trejo, A. Roman-Flores, Additive manufacturing and viscoelasticity evaluation of Bézier metamaterials fabricated via vat photopolymerization, Addit. Manuf. 60 (2022) 103281.
[42] K. Zhang, C. Zhao, P. Zhao, J. Luo, Z. Deng, Wave propagation properties of rotationally symmetric lattices with curved beams, J. Acoust. Soc. Am. 148 (3) (2020) 1567–1584.
[43] S. Mukherjee, M. Cajić, D. Karličić, S. Adhikari, Enhancement of band-gap characteristics in hexagonal and re-entrant lattices via curved beams, Compos. Struct. 306 (2023) 116591.
[44] A. Harkati, E.H. Harkati, A. Bezazi, F. Scarpa, M. Ouisse, Out-of-plane elastic constants of curved cell walls honeycombs, Compos. Struct. 268 (2021) 113959.
[45] D.P. Kingma, M. Welling, Auto-encoding variational Bayes, in: Y. Bengio, Y. LeCun (Eds.), 2nd International Conference on Learning Representations, ICLR 2014, Banff, AB, Canada, April 14–16, 2014, Conference Track Proceedings, 2014.
[46] I. Goodfellow, J. Pouget-Abadie, M. Mirza, B. Xu, D. Warde-Farley, S. Ozair, A. Courville, Y. Bengio, Generative adversarial networks, Commun. ACM 63 (11) (2020) 139–144.

[47] L. Wang, Y.-C. Chan, F. Ahmed, Z. Liu, P. Zhu, W. Chen, Deep generative modeling for mechanistic-based learning and design of metamaterial systems, Comput. Methods Appl. Mech. Engrg. 372 (2020) 113377.
[48] J. Wang, W.W. Chen, D. Da, M. Fuge, R. Rai, IH-GAN: A conditional generative model for implicit surface-based inverse design of cellular structures, Comput. Methods Appl. Mech. Engrg. 396 (2022) 115060.
[49] S. Kumar, S. Tan, L. Zheng, D.M. Kochmann, Inverse-designed spinodoid metamaterials, npj Comput. Math. 6 (2020) 73.
[50] J.-H. Bastek, S. Kumar, B. Telgen, R.N. Glaesener, D.M. Kochmann, Inverting the structure–property map of truss metamaterials by deep learning, Proc. Natl. Acad. Sci. 119 (1) (2022) e2111505119.
[51] T.J.R. Hughes, J.A. Cottrell, Y. Bazilevs, Isogeometric analysis: CAD, finite elements, NURBS, exact geometry and mesh refinement, Comput. Methods Appl. Mech. Engrg. 194 (39) (2005) 4135–4195.
[52] K.A. Johannessen, E. Fonn, Splipy: B-spline and NURBS modelling in Python, J. Phys. Conf. Ser. 1669 (2020) 012032.
[53] D.E. Rumelhart, G.E. Hinton, R.J. Williams, Learning representations by back-propagating errors, Nature 323 (1986) 533–536.
[54] D.P. Kingma, J. Ba, Adam: A method for stochastic optimization, in: Y. Bengio, Y. LeCun (Eds.), 3rd International Conference on Learning Representations, ICLR 2015, San Diego, CA, USA, May 7-9, 2015, Conference Track Proceedings, 2015.
[55] L.J. Ba, J.R. Kiros, G.E. Hinton, Layer normalization, CoRR, 2016, abs/1607.06450.
[56] J. Schindelin, I. Arganda-Carreras, E. Frise, V. Kaynig, M. Longair, T. Pietzsch, S. Preibisch, C. Rueden, S. Saalfeld, B. Schmid, J.-Y. Tinevez, D.J. White, V. Hartenstein, K. Eliceiri, P. Tomancak, A. Cardona, Fiji: an open-source platform for biological-image analysis, Nature Methods 9 (7) (2012) 676–682.